Enhancing properties with distortion: A comparative study of two iron-phosphide Fe_2P polymorphs

Seongyoung Kong,[a,b] Prashant Singh,[b] Arka Sarkar,[a,b] Gayatri Viswanathan,[a,b] Yury V. Kolen'ko,[c] Yaroslav Mudryk,[b] Duane D. Johnson,[b,d] Kirill Kovnir[a,b,*]

[a] *Department of Chemistry, Iowa State University, Ames, IA 50011, USA*

[b] *Ames National Laboratory, U.S. Department of Energy, Ames, IA 50011, USA*

[c] *Nanochemistry Research Group, International Iberian Nanotechnology Laboratory, Braga 4715-330, Portugal*

[d] *Department of Materials Science & Engineering, Iowa State University, Ames, IA 50011, USA*

Corresponding author: kovnir@iastate.edu

ABSTRACT

Iron phosphide (Fe_2P) crystallizes in its own hexagonal crystal structure type (h-Fe_2P). As found in meteorites, orthorhombic polymorph (o-Fe_2P) was originally reported as a high-temperature and high-pressure phase. Recently, o-Fe_2P was described as stable at ambient pressure, yet no synthetic methods were developed for single-crystal growth or single phase bulk powder synthesis. Here, we report a successful method for growing o-Fe_2P single crystals and synthesizing phase-pure polycrystalline samples using tin-flux. *In situ* powder X-ray diffraction studies showed that the phase transition from o-Fe_2P to h-Fe_2P occurs around 873 K and, below that temperature, the formation of the o-Fe_2P phase is favored thermodynamically rather than kinetically. Systematic comparison of transport, magnetic, and electrocatalytic properties of both h-Fe_2P and o-Fe_2P phases showed a substantial impact of the crystal structure on properties. The orthorhombic structural distortion resulted in considerable changes in magnetic properties with the o-Fe_2P phase exhibiting a 60% lower Fe magnetic moment and a substantially higher ferromagnetic Curie temperature than h-Fe_2P. Electrochemical measurements towards hydrogen-evolution reaction in acidic media showed that the o-Fe_2P phase requires 80 mV lower overpotential than h-Fe_2P phase to generate a current density of –10 mA/cm^2, and their electronic structures suggest that the higher density of states at the Fermi energy is the origin of superior catalytic activity in o-Fe_2P.

INTRODUCTION

Transition-metal phosphides exhibit great versatility in terms of composition and structures. The transition metal to phosphorous ratio can vary from 7.5:1 ($Pd_{15}P_2$) to 1:10 (Cu_2P_{20}) in binary phases. Metal-rich compounds may have more than 10 metal atoms surrounding one P. In turn, P-rich compounds show diverse 0-, 1-, 2-, and 3-D polyanionic building blocks due to extensive P–P bonding, such as dumbbells, chains, rings, and cages.[1–4] Due to the diversity of crystal structures and resulting properties, metal phosphides have been adapted for a myriad of applications, including superconductors, supercapacitors, thermoelectrics, rechargeable batteries, magnets, optoelectronics, biomedicine, and (photo)(electro)catalysts.[5–15] Recently, phosphides of earth-abundant transition-metals have gained huge attention as water-splitting catalysts due to their good chemical stability in acidic/alkaline electrolytes and high catalytic activity.

Fe_2P is an interesting material as it is one of the few phosphides that exhibits ferromagnetism with large anisotropy.[16–21] *h*-Fe_2P has been known to crystallize in the hexagonal structure type (Fe_2P, space group: $P\bar{6}2m$, Pearson symbol: *hP*-9) at ambient condtions.[22,23] When it is doped with Mn and As, it displays a huge magnetocaloric effect.[24] Fe_2P has been of interest to geologists as there are few reported iron-phosphide phases in meteorites, such as barringerite [$(Fe,Ni)_2P$, space group: $P\bar{6}2m$], giving hints of a metastable environment when it was formed.[25–27] In 2002, a new orthorhombic polymorph of iron meteorite, allabogdanite [$(Fe,Ni)_2P$, space group: *Pnma*], was found in Onello meteorite,[28,29] and it stimulated the study of orthorhombic Fe_2P phase (*o*-Fe_2P). Although it was first reported that this phase was generated under a high pressure of 8 GPa and high temperature of 1400 K,[29–32] Litasov and co-workers recently showed that allabogdanite and Ni-free Fe_2P with the same structure could be stable at ambient pressure.[33] The *o*-Fe_2P phase was first introduced by Senateur and co-workers in 1976,[34] yet to date there are few reports about predicting the phase stability or analyzing the magnetic properties of *o*-Fe_2P phase at high pressure,[31,34–37] and many of intrinsic properties of *o*-Fe_2P at ambient pressure remain hidden.

The comparative study of polymorphs can be useful to investigate the effect of bulk structure on materials properties.[38–42] Polymorphs can have similar properties or may show drastic differences. For instance, β-Ca_2CdP_2 displays a superior second-harmonic generation intensity over α-Ca_2CdP_2 due to the higher degree of distortion in CdP_4 tetrahedral layers.[43] The $CuSe_2$ with pyrite crystal structure shows superconductivity at a higher temperature than $CuSe_2$ marcasite phase.[44,45] The semi-metallic nature of the cubic NiP_2 polymorph requires less overpotential for hydrogen/oxygen evolution reactions (HER/OER) than for the semiconducting monoclinic NiP_2 phase.[46] Polymorphism can also significantly vary the transport properties of complex ternary and quaternary materials, such as clathrates or tetrel-phosphides.[6,40,47] The violet-P_{11} polymorph of phosphorus shows a bandgap >2.0 eV, which is considerably larger than for other white or red P allotropes.[48] Many new polymorphs can be made using different flux media or low temperature profiles to access metastable phases.[49] Another common method is to apply high pressure or high temperature, such as during the syntheses of orthorhombic NiP or hexagonal Co_2P phases.[50–52] Many polymorphs of binary metal phosphides are known but reports on their properties are still rare as the synthesis of single-phase materials at ambient pressures is challenging, and has yet to be realized.

In this study, *o*-Fe_2P polymorph (structure type: TiNiSi, space group: *Pnma*, Pearson symbol: *oP*–12) was investigated and compared to the *h*-Fe_2P polymorph in terms of transport, magnetic, and electrocatalytic properties. The single-crystal growth and single-phase powder synthesis of *o*-Fe_2P phase were achieved via tin-flux method under ambient pressure. An *in situ* X-ray diffraction study was performed to understand the mechanism of *o*-Fe_2P phase formation and the phase transition to *h*-Fe_2P. We demonstrated that the crystal structure change from *h*-Fe_2P to *o*-Fe_2P modifies the electronic structure, transport, and magnetic properties. The differences in electrocatalytic activity towards hydrogen evolution reaction showed that the bulk structure is important to control the activity of a chemical reaction on the surface facets, which is corroborated by theoretical insights.

EXPERIMENTAL SECTION

Synthesis of *h*–Fe_2P and *o*–Fe_2P polymorphs

Fe powder (99.9%, Alfa Aesar), red phosphorus (98.7%, Alfa Aesar), CsCl (99.99%, Sigma Aldrich), and Sn shot (99.8%, Alfa Aesar) were utilized for Fe_2P polymorphs synthesis.

Sn-flux method. To synthesize the *o*–Fe_2P phase, the molar ratio of Fe:P:Sn was 6:3:10, and the total reaction scale was 1 g. Increasing the ratio of Sn resulted in formation of the hexagonal phase. All elements were loaded in the 9/11 mm (I.D./O.D.) clear fused-silica ampoule, followed by placing a silica wool plug and small silica pieces on top to retrieve the sample after high-temperature centrifugation. Next, the reaction ampoule was evacuated and then flame-sealed. In a muffle furnace, the sample was heated to 600 °C in 10 h and dwelled for 72 h, followed by centrifuging the molten flux. The ampoule was opened in the air, and the sample was immersed in the 1:1 ratio of HCl/H_2O solution overnight to remove any residual Sn. After the sample was filtered, it was dried in air overnight. A gray chunk of *o*-Fe_2P was obtained.

For the *h*-Fe_2P phase synthesis, the molar ratio of Fe:P:Sn was 6:3:90 and the total reaction scale was 4 g. The sample was prepared in the same way as for the *o*–Fe_2P reaction, and the ampoule was heated to 850 °C in 12 h and dwelled for 72 h, followed by centrifuging the liquefied Sn. The product was collected by opening the reaction ampoule in the air, followed by the same acidic washing procedure to remove the remaining Sn. After filtering and drying, a gray sample of *h*-Fe_2P was obtained.

Element or salt-flux method. The *o*-Fe_2P phase was also prepared without Sn-flux by reacting stoichiometric amounts of Fe and P in a 300 mg total scale. The sample was loaded in 9/11 mm (I.D./O.D.) silica ampoule without silica wool/silica pieces and flame sealed after evacuation. The temperature profile was heating to 600 °C in 10 h, dwelling for 72 h, and natural cooling by turning off the furnace. The ampoule was opened in the air and the product was collected.

The *h*-Fe_2P phase was also synthesized using salt flux. The ratio of Fe:P was 2:1.03 (Fe+P was 300 mg) with 600 mg of CsCl salt flux added. All reactants were loaded in the silica ampoule, evacuated, and flame sealed. The sealed reaction ampoule was heated to 800 °C for 12 h, followed by dwelling for 72 h, and naturally cooled down. The ampoule was opened in ambient conditions, and sample was immersed in water for 2 h to remove the salt. After filtering, the sample was dried in the air overnight. A dark gray powder of *h*-Fe_2P was obtained.

Powder X-ray diffraction (PXRD)

For PXRD, a bench top MiniFlex600 diffractometer (Rigaku) with a Cu-K_α X-ray source (λ = 1.540593 Å) and a Ni-K_β filter was used. A Si holder with zero background was utilized for powder sample characterization. Fluorescence reduction was applied during the measurement.

Single crystal X-ray diffraction (SCXRD)

Single crystals of *h*-Fe_2P and *o*-Fe_2P were analyzed by D8 Venture diffractometer (Bruker) with Mo-K_α radiation. Data were collected with a 0.3° step of φ and ω scans at 173 K and integrated using the APEX3 software package (Bruker). For further structure solution and refinement, the SHELX suite was utilized.[53]

Scanning electron microscopy (SEM) and energy dispersive X-ray spectroscopy (EDX)

To obtain images and compositional information of the *o*-Fe_2P single crystal, a JSM-IT200 (JEOL) with built-in EDX was utilized under 15 kV accelerating voltage. The data was processed with the SMILE VIEW software package (JEOL). To acquire the surface image of the pellets, a Quanta 250 field emission SEM (FEI) was utilized at 15 kV accelerating voltage.

In situ **PXRD**

In situ PXRD data were collected at beamline 17-BM at the Advanced Photon Source at Argonne National Laboratory. To investigate the synthesis processes, two different compositions were prepared: Fe, P, and Sn in a 6:3:10 molar ratio and Fe and P in a 2:1 molar ratio. Each mixture of elements was ground together in the mortar and loaded in the 0.5/0.7 mm (I.D./O.D.) quartz capillary and then flame-sealed after evacuation. The capillary was placed between two heating coils, and the thermocouple was placed outside the tip of the reaction capillary. For both samples, the temperature profile was heating to 300 °C with a rate of 20 °C/min, then heating to 600 °C with a rate of 10 °C/min, dwelling for 15 min, and finally natural cooling with heating turned off. Diffraction data were acquired every 60s.

To investigate the phase transition, a third capillary was loaded with single-phase *o*-Fe_2P powder, evacuated, and flame-sealed. The heating profile was heating to 400 °C with a rate of 30 °C/min, then heating to 750 °C with a rate of 10 °C/min, then cooling to 500 °C with a rate of 20 °C/min, and finally natural cooling. The collected data were integrated and processed with GSAS II software package.[54]

Differential scanning calorimetry (DSC)

Thermal behavior was studied using a DSC 404 F3 Pegasus (Netzsch) high-temperature differential scanning calorimeter. 20 mg of *o*-Fe_2P was loaded in a 5/7 mm (I.D./O.D.) silica ampoule, evacuated, and flame sealed. For background correction, a similar size empty ampoule was utilized. The individual sample was heated to 400, 500, 550, 600, and 1100 °C, respectively, at the rate of 10 °C/min, and cooled down to room temperature at the same rate. After DSC measurement, the sample was further analyzed by PXRD.

Spark plasma sintering (SPS)

To consolidate the powdered samples into dense pellets, a Dr Sinter Lab Jr. SPS-211Lx (Fuji Electronics Industry Co., Ltd.) was utilized. 4 mm tungsten-carbide plungers and die were used. Between the sample and plunger, two pieces of graphite sheet were placed. The die assembly was placed in the SPS chamber and evacuated. When the pressure reduced < 1.0 Pa, evacuation was stopped, and Ar gas was partially filled to suppress the possible vaporization of phosphorous during the sintering. Initially, a pressure of 160 MPa was applied to the pellet to increase the thermal contact of the sample. Then, the sample was heated to 300 °C for 4 min and dwelled for 10 min. When the temperature reached 300 °C, the pressure gradually increased to 800 MPa, and it was released as soon as dwelling was completed. The sample was allowed to cool down naturally. The SPSed pellet was further polished using 600, 1500, and 2500 grits of sandpaper, respectively. The geometric density of the pellets was estimated to be 75% for both Fe_2P polymorphs for transport property measurements, as well as 84% for *h*-Fe_2P and 80% for *o*-Fe_2P for electrochemical measurements.

Transport measurements

To characterize the physical transport properties of the two Fe_2P polymorphs from 10 to 300 K, a physical property measurement system (PPMS, Quantum Design) was used. The SPSed pellet was attached to the gold leads in a two-probe system using an H20E conductive epoxy (Epoxy Technology) to measure the thermal conductivity and Seebeck coefficient. After that, the pellet was cut into a bar shape to measure electrical resistivity. The electrical resistivity was conducted with a four-probe system by attaching 50 μm platinum wires to the bar using conductive silver paste.

Magnetic measurements

Magnetic properties of the polycrystalline powders were measured by a MPMS-XL SQUID magnetometer (Quantum Design). The temperature dependence of the magnetic susceptibility was measured from 2 K to 320 K at an applied magnetic field of 0.1 T. The isothermal magnetization field dependence was measured from –7 T to 7 T at 2 K and 300 K. 31.8 mg of *h*-Fe_2P and 33.3 mg of *o*-Fe_2P were used for the measurements.

Cathode fabrication

To perform electrocatalytic testing, cathode was fabricated from the SPS-ed pellets. An assembly was made by attaching the pellet and Au wire (99.95%, 100 μm, ThermoScientific Chemicals) using an H20E conductive epoxy (Epoxy Technology), followed by curing at 150 °C for 1 h. Then, it was molded in the non-conductive epoxy to protect the joint parts from the electrolyte. A Teflon rod was also molded with the assembly to assist holding the cathode with clamp. Once the epoxy was cured, the surface of the pellet to be exposed to electrolyte was polished using 300, 600, and 1500 grits of sandpaper, respectively. After that, the surface of the cathode was further polished by alumina suspensions of 1.0, 0.3, and 0.05 μm, respectively, and with the cathode being sonicated with water and ethanol for 5 min and 3 min, respectively, between the polishing steps.

Electrochemical measurements

Electrochemical properties of the synthesized materials towards acidic HER were investigated in a three-electrode system. A calibrated saturated calomel electrode (SCE) was used as a reference electrode, a as-fabricated cathode as a working electrode, and a polished and cleaned graphite rod as a counter electrode. 0.5 M H_2SO_4 was utilized as the electrolyte and hydrogen gas was purged for 30 min prior to the electrochemical measurement. The scan rate of cyclic voltammetry (CV) and linear sweep voltammetry (LSV) was 5 mV/s in the potential range from $-0.25\ V_{SCE}$ to $0.85\ V_{SCE}$, and the 85% of iR_u voltage drop correction was applied. The solution resistance (R_u) value was obtained from the highest frequency data point of Nyquist plot measured from electrochemical impedance spectroscopy (EIS). The EIS measurement was conducted at $-0.510\ V_{SCE}$ with 5 mV of AC amplitude in the frequency range from 10^5 to 10^{-2} Hz. To stabilize the sample, HER activity was recorded after a span of three days measurement, with 50 cycles conducted each day. The following equation was used to convert the SCE potential to the reversible hydrogen potential E_{RHE}: $E_{RHE} = E_{SCE} + 0.244\ V + 0.059\times pH$

To measure HER stability of samplese, accelerated degradation testing (ADT) of samples was performed with a scan rate of 50 mV/s in the potential range from $-0.25\ V_{SCE}$ to $0.65\ V_{SCE}$ for a continuous 1,000 cycles. Chronopotentiometry (CP) was also performed as a durability test, in which the overpotential (η_{10}) to generate current density $j = -10$ mA/cm^2 was monitored during 20 h.

Density functional theory (DFT) calculations

DFT as implemented in Vienna *ab initio* simulation package (VASP) was used for electronic-structure calculation based on the Perdew, Burke, and Ernzerhof (PBE) exchange-correlation functionals.[55–57] Full relaxation (volume and atomic coordinates) was performed until energy and forces converged to 10^{-6} eV and 10^{-3} eV/Å, respectively. A kinetic-energy cutoff of 520 eV was used for the plane-wave basis set. Spin-polarized calculations were performed due to the presence of Fe magnetism in both Fe_2P polymorphs. Monkhorst-Pack *k*-mesh grids of 3×3×6 and 4×6×3 were used to sample the Brillouin zone in hexagonal and orthorhombic phase, respectively, during relaxation, while the mesh-size was doubled to accurately determine formation enthalpy and electronic-structure properties. The bonding analysis was performed using projected crystal orbital Hamilton population (pCOHP), as implemented in Local Orbital Basis Suite Towards Electronic Structure Reconstruction code (LOBSTER).[58–60] The projected COHP is a modern variant of the traditional COOP technique in which the off-site densities-of-states are weighted by the respective Hamilton matrix elements to reveal bonding, nonbonding, and antibonding interactions.[61,62]

RESULTS AND DISCUSSION

Synthesis

We synthesized the *o*-Fe_2P phase during attempts to make a ternary Mg-Fe-P compound at 600°C, and this temperature appeared to be optimum for the synthesis of *o*-Fe_2P, similar to the previous report.[33] We originally suspected that Mg might stabilize the *o*-Fe_2P phase but later found that *o*-Fe_2P can be formed in Mg-free conditions using tin-flux or just from elements. The formation of *o*-Fe_2P in a direct reaction of elements confirms that Sn is not incorporated in the crystal structure but rather serves as reaction media **(Figure S1)**. From different synthesis attempts, the Sn-flux method was the most reproducible in forming single-phase *o*-Fe_2P bulk powder. The Sn-flux method is useful for low-temperature polymorphs or metastable-phase syntheses as Sn has a low melting point of 232°C and dissolution of elements in molten tin accelerates the diffusion between the reactants.[46,49,63,64] *o*-Fe_2P sample synthesized via direct reaction of elements contained an admixture of *h*-Fe_2P **(Figure S1)**.[33] **Figure 1b** shows that the PXRD pattern of *o*-Fe_2P matches the calculated one well. Single phase *h*-Fe_2P was also synthesized using Sn-flux but at a higher temperature of 850 °C, as shown in **Figure 1a**. The formation of different polymorphs at different temperatures under otherwise the same synthetic condition indicates that *o*-Fe_2P is a low-temperature polymorph. A Rietveld refinement was conducted on the PXRD pattern of *o*-Fe_2P to confirm the crystal structure and single phase nature (**Figure 1c**). Moreover, a single crystal of *o*-Fe_2P was collected from the same batch. **Figures 1d,1e** show the scanning electron microscopy (SEM) image and energy-dispersive X-ray spectroscopy (EDX) results of the *o*-Fe_2P single crystal. They display that there were no additional elements present, such as Sn from the flux or Si from the reaction ampoule to stabilize the orthorhombic crystal structure. It conforms to the previous stability calculation that *o*-Fe_2P is a stable phase at ambient conditions.[36,37] Previously, an *o*-Fe_2P single crystal was obtained through a transformation of the *h*-Fe_2P single crystal after applying high pressure and temperature.[30] Our results demonstrate that *o*-Fe_2P single crystals can be grown at ambient pressure and low temperature through the Sn-flux method.

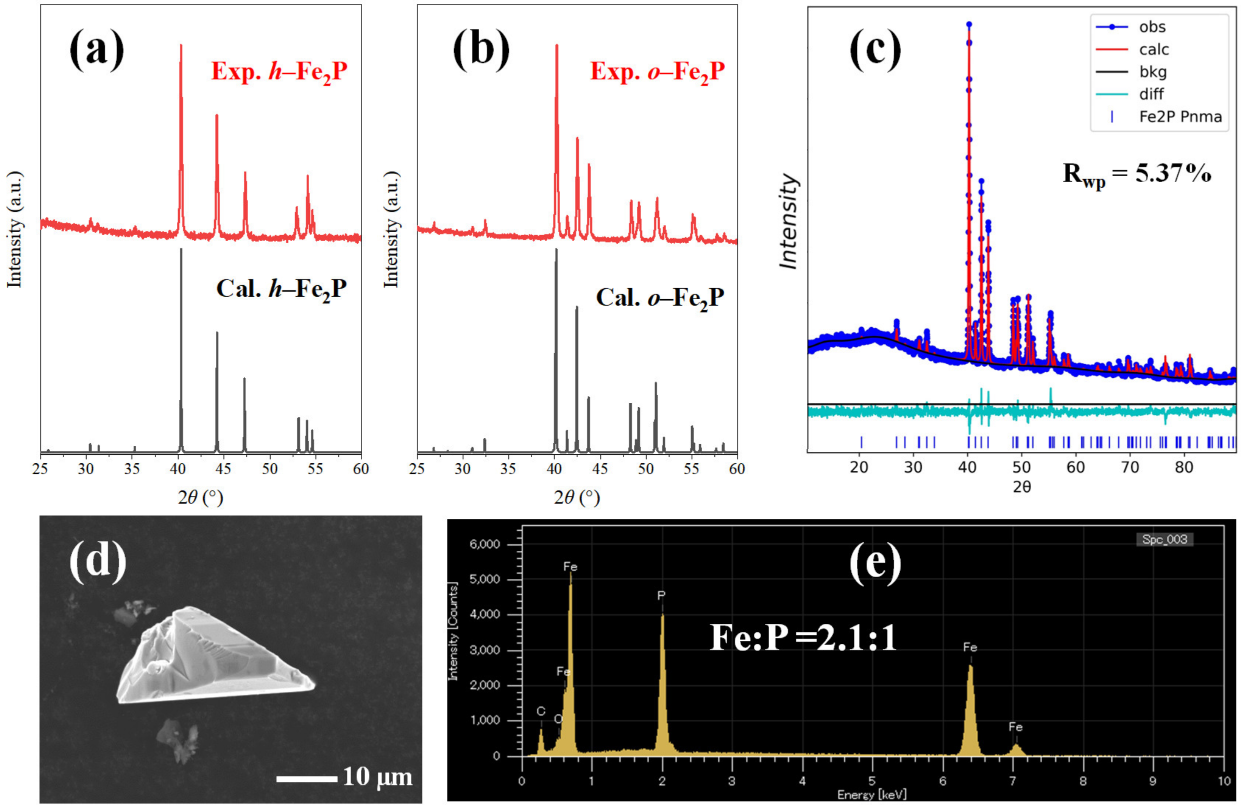

Figure 1. Calculated (black) and experimental (red) PXRD patterns of (a) *h*-Fe_2P and (b) *o*-Fe_2P phases synthesized using tin-flux. Calculated patterns were derived from SCXRD data. (c) Rietveld refinement of *o*–Fe_2P PXRD pattern. Representative (d) SEM image and (e) EDX spectrum of *o*-Fe_2P single crystal.

Table 1. Crystallographic refinement parameters for *h*-Fe_2P and *o*-Fe_2P.

Compound	***h*–Fe_2P**	***o*–Fe_2P**
temperature (K)	173	
radiation (Å)	Mo-K_α, 0.71037	
crystal system	hexagonal	orthorhombic
space group	$P\bar{6}2m$ (no. 189)	*Pnma* (no. 62)
a [Å]	5.8724(3)	5.7810(7)
b [Å]		3.5726(4)
c [Å]	3.4445(2)	6.6486(8)
Volume [$Å^3$]	102.87(1)	137.31(3)
Z	3	4
Volume/*Z* [$Å^3$]	34.290(3)	34.33(1)
data/parameters	171/13	285/19
density (g/cm^3)	6.909	6.901
u (mm^{-1})	21.55	21.53
R_{int}	0.032	0.022
GOF	1.11	1.10
R_1 [$I > 2\sigma(I)$]	0.013	0.026
wR_2 [$I > 2\sigma(I)$]	0.033	0.062

R_1	0.014	0.031
wR_2	0.033	0.062
diff. peaks [e A^{-3}]	0.55/–0.31	1.22/–1.23

Crystal structure

The single-crystal X-ray diffraction (SCXRD) data and refinement results for *h*-Fe_2P and *o*-Fe_2P are summarized in **Table 1**, with additional details listed in **Tables S1–S3**. Notably, *o*-Fe_2P has a slightly larger volume per formula unit than that of *h*-Fe_2P phase. In previous studies performed at high pressure of 8 Ga and temperature of 800°C, the formula unit volume of *o*-Fe_2P phase (34.24 Å^3) was reported to be slightly smaller than that of *h*-Fe_2P (34.36 Å^3).[30,34] Compared to reported isostructural orthorhombic Co_2P, the unit-cell volume of *o*-Fe_2P is 4.6% larger.[65] *h*-Fe_2P and *o*-Fe_2P crystal structures have two inequivalent Fe sites, but *h*-Fe_2P has two P sites while *o*-Fe_2P has only one P site. In both polymorphs, Fe1 is tetrahedrally coordinated by P and Fe2 has a square-pyramidal coordination with P. When P is considered as a central atom, all P sites in both polymorphs have a tricapped trigonal prism coordination with 9 Fe atoms (**Figure 2**). In *h*-Fe_2P, the polyhedral volume of P1@Fe_9 is 28.26 Å^3 with an average P1–Fe bond length of 2.390 Å, while that of P2@Fe_9 is 24.92 Å^3 with an average P2–Fe bond length of 2.323 Å. Along the [0001] direction, P1@Fe_9 polyhedra in *h*-Fe_2P are arranged in columns by sharing the Fe2 trigonal faces, while P2@Fe_9 polyhedra form columns by sharing the Fe1 trigonal faces. Both polyhedra types tile the space alternatively by sharing edges along the *a* and *b* axes. In *o*-Fe_2P structure, there is only one type of P@Fe_9 polyhedra (**Figure 2b**). This polyhedron is more distorted than the analogous polyhedra in the hexagonal structure. P@Fe_9 has an intermediate volume of 26.99 Å^3 with an average P–Fe bond length of 2.373 Å, values between that for P1@Fe_9 and P2@Fe_9 polyhedra in *h*-Fe_2P. The *h*-Fe_2P structure has a total of four different Fe–Fe shortest distances, ranging from 2.615 Å for Fe1–Fe1 to 3.085 Å for Fe2–Fe2 (**Figure 2c**). The *o*-Fe_2P structure has a total of seven different Fe–Fe bond distances, ranging from 2.584 Å for Fe1–Fe1 to 3.092 Å for Fe2–Fe2 (**Figure 2d**). In both structures, the Fe1–Fe1 bond is the shortest, the Fe2–Fe2 bond is the longest, and Fe1–Fe2 bonds are at intermediate interatomic distances.

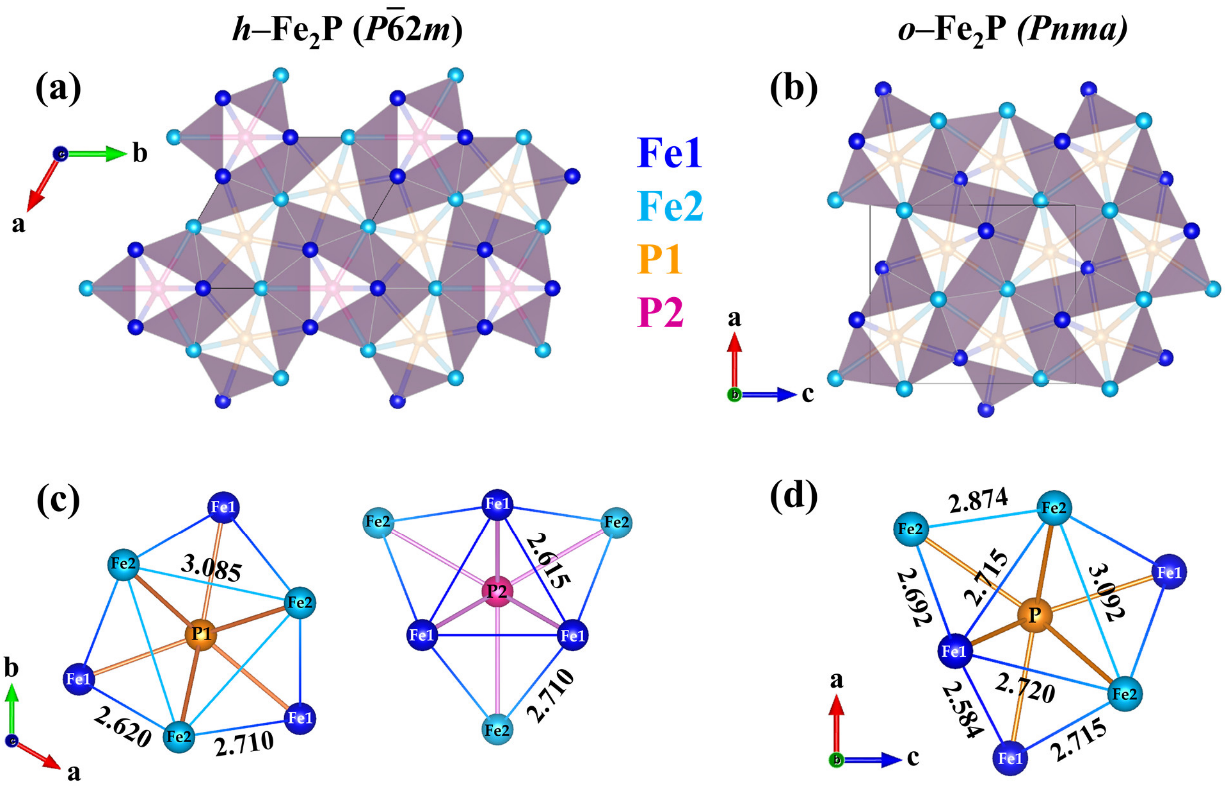

Figure 2. Crystal structure of (a,c) *h*-Fe_2P and (b,d) *o*-Fe_2P. (a) and (b) show the polyhedral structure emphasizing P@Fe_9 polyhedra, while (c) and (d) show the Fe–Fe distances in each polyhedron.

In situ PXRD

To investigate the synthesis process of the *o*-Fe_2P polymorph, heat-induced phase transformations in two different samples, Fe+P and Fe+P+Sn, were studied by *in situ* variable-temperature PXRD. **Figure S2a** shows the contour plot of the Sn-flux reaction upon the following temperature profile: heating to 600°C for 45 min, dwelling for 15 min, and natural cooling to room temperature. Notably, 600°C is the temperature used for *ex situ* *o*–Fe_2P synthesis, but the reaction time was significantly shortened due to limited available beamtime. The enlisted temperatures next to the plot are approximate (± 20°C) because the thermocouple was placed outside of the reaction tube. Upon heating of the Sn-containing sample, the formation of Sn_4P_3 at ~330°C was observed as an intermediate phase followed by a reaction with Fe resulting in the formation of the *h*-Fe_2P phase at ~450°C. FeSn and FeP were also observed as intermediate phases, but they were completely reacted as temperature increased, and turned into *h*-Fe_2P (major) and Fe_3P (minor) phases once the reaction was cooled down. Interestingly, even during the 15 min dwelling process at 600°C, no *o*-Fe_2P phase was observed. Provided that the *in situ* reaction dwell time of 15 min is much shorter than actual synthesis time of 72 h, it could indicate that *h*-Fe_2P is a kinetically favorable phase while *o*-Fe_2P is a thermodynamically favorable phase at 600 °C. *In situ* studies of the reaction of Fe+P elements without flux following the same temperature profile showed similar trends (**Figure S2b)**. During the reaction, the only intermediate phase detected was FeP, and the final product was a mixture of *h*-Fe_2P, Fe_3P, and unreacted Fe. The amounts of Fe_3P in the products was higher in the reaction of elements without flux and, in a previous study, elemental Fe was not fully reacted even for 15 days of annealing at 500°C.[33] Hence, these *in situ* studies emphasize the role of tin as a good media to homogenize/facilitate this reaction.

The phase transformation of *o*-Fe_2P into *h*-Fe_2P was also investigated (**Figure 3a)**. Due to substantial diffraction peak overlaps, distinct peaks, i.e, ones specific for each phase, were selected for analysis (**Figure 3b).** The peak of *h*-Fe_2P located at 3.07 $Å^{-1}$ becomes noticeable at 651°C, and it intensified with increasing temperature up to the maximum used temperature of 750°C. Upon cooling, this peak intensity is maintained, and the *h*-Fe_2P is a major phase in the resulting sample. The identity peak of *o*-Fe_2P at 2.95 $Å^{-1}$ starts decreasing once temperature exceeds 600°C and doesn't increase during the cooling. This result suggests that the phase transformation from *o*-Fe_2P to *h*-Fe_2P occurs above 650°C, and the reverse transformation from *h*-Fe_2P to *o*-Fe_2P is a much slower process, if it occurs at all (**Figure 3c).** The *h*/*o* ratio was calculated by integrating the area of two selected peaks shown in **Figure 3b** as dashed lines. The *h*/*o* ratio is almost zero at room temperature, and it drastically increases after 650°C, and the rate of transformation reaches the maximum at 750 °C, and then slows down upon cooling. During the cooling process, the ratio remains almost the same at about 1.8 after 600 °C. A complete $o \rightarrow h$ transformation was not achieved, probably due to short time that the sample was exposed to $T > 650$°C, namely 15 min. These transformation results corroborate that *h*-Fe_2P is a high-temperature polymorph. A similar phase relation was reported for Co_2P, where *h*-Co_2P is a high-temperature polymorph stable above 1150°C, while *o*-Co_2P is the low-temperature polymorph.[65]

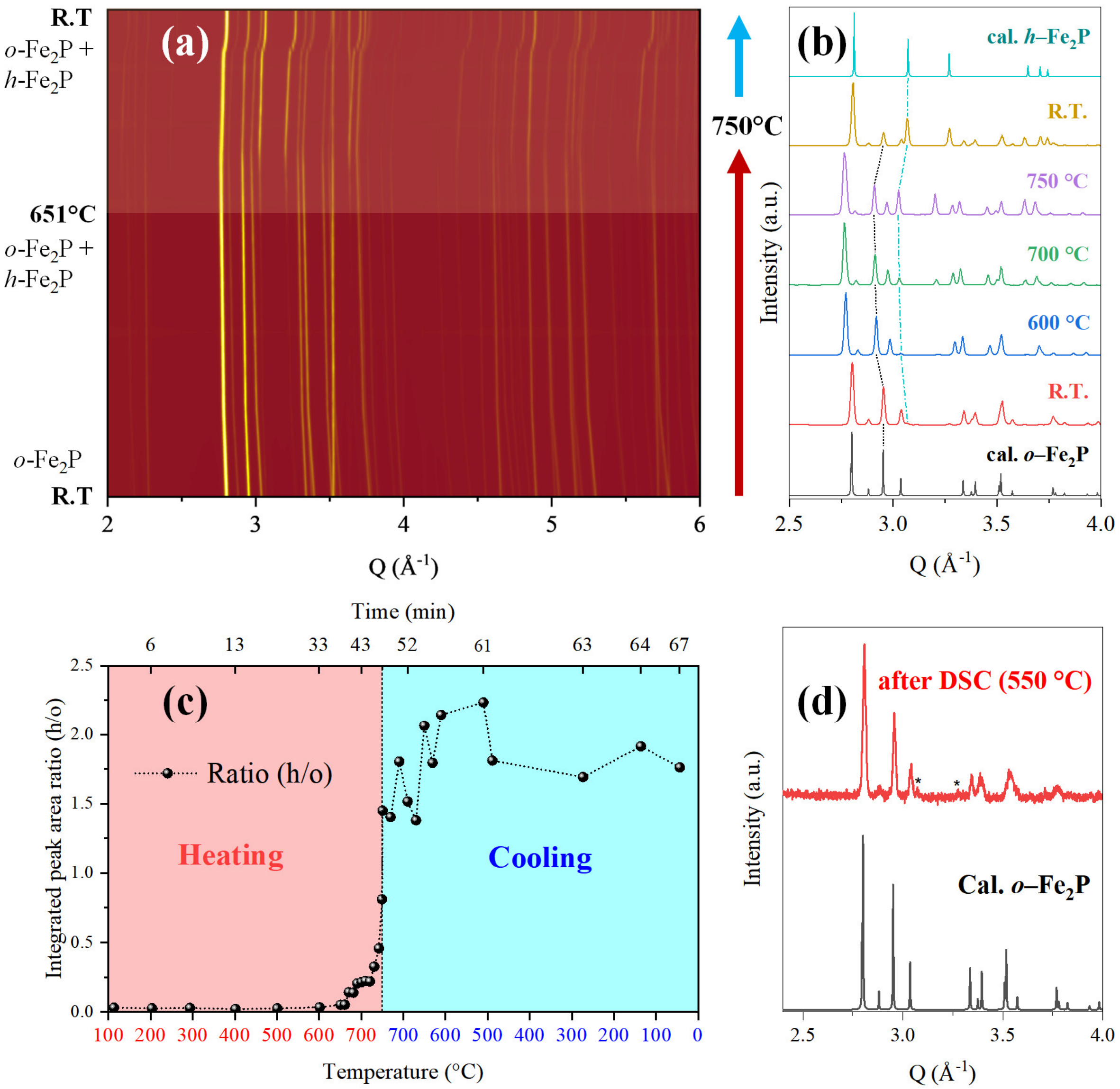

Figure 3. Contour plot (a) and selected diffraction patterns (b) of *in situ* PXRD measurements of the phase transformation from *o*-Fe_2P to *h*-Fe_2P. The red arrow on the right side of the plot indicates the heating while the blue one indicates the cooling process. The phases detected at the corresponding temperature are listed on the left side of the plot. In (b), the thermal shift of the two selected peaks used for the *h*/*o* ratio quantification are marked with dashed lines. (c) The ratio of *h*-Fe_2P to *o*-Fe_2P as a function of temperature. (d) PXRD pattern of *o*-Fe_2P phase after DSC measurement with the highest temperature of 550 °C. Asterisk in (d) indicate peaks of the *h*-Fe_2P phase.

The o-Fe_2P was further analyzed by differential scanning calorimetry (DSC), and no observable peaks were detected during the four different temperature scans (**Figure S3a**). PXRD analysis of the samples after DSC detected the formation of h-Fe_2P in the experiment with maximum temperature of 550°C, as shown in **Figures 3d, S3b**. However, no transformation to h-Fe_2P was observed after DSC below 500°C. A complete $o \rightarrow h$ transformation occurs due to DSC experiment with maximum temperature of 1100°C. To determine whether the $o \rightarrow h$ transformation occurs as a slow process at lower temperatures, the o-Fe_2P phase was dwelled at either 400°C or 500°C for 20 days; in both cases the hexagonal phase did not appear **(Figure S4a)**. The DSC and dwelling process studies indicate that the transformation of o-Fe_2P to h-Fe_2P starts as low as 550°C, in line with the *in situ* PXRD data. The reversibility of the $h \rightarrow o$ transformation was probed by annealing h-Fe_2P at 400 and 500°C for 25 days (**Figure S4b**). No o-Fe_2P phase was detected in the products of such heat treatments, which is consistent with the previous report.[33] We hypothesize that at temperatures below 550°C the h-Fe_2P phase is kinetically stabilized due to the high activation barrier required to transform it to the o-Fe_2P.

Phase stability, electronic structure, and bonding analysis

The DFT formation energy at 0 K ($E_{form} = E_{tot} - \sum_i n_i E_i, i = Fe, P$) was used to assess the stability of Fe_2P in orthorhombic and hexagonal forms, including considering ferro-magnetic (FM) vs. non-magnetic (NM) states. The E_{tot} is total energy of o/h-Fe_2P while $\{n_{i,}\ E_i\}$ are number of atoms of type "i" in the unit cell and the respective energies for specific magnetic states. The E_{form} of FM-Fe_2P was found to be –372.2 meV/atom for orthorhombic and –351.4 meV/atom hexagonal phases, reflecting the favorable formation of FM-Fe_2P compounds. The o-Fe_2P phase is more stable than h-Fe_2P by 20.8 meV/atom, which is consistent with the thermodynamic stability of the orthorhombic polymorph from synthesis and experimental thermal studies here and from previous stability calculation reports.[36,37] For completeness, the E_{form} of NM-Fe_2P was found to be –330.3 meV/atom for orthorhombic and –327.5 meV/atom for hexagonal phases, indicating that the FM state is favored at lower temperatures. For the non-magnetic states, the energy difference is only 2.8 meV/atom and it is reasonable that at elevated temperatures, in the paramagnetic state, the hexagonal phase becomes more stable.

To understand the electronic structure of the two Fe_2P polymorphs, spin-polarized DFT results were used to analyze the density of states (DOS), as presented in **Figure 4**. We found that *o*-Fe_2P phase has a more symmetric contribution of spin-up (majority) and spin-down (minority) states at the Fermi energy (E_F) compared to that of the *h*-Fe_2P phase, comparing **Figures 4a,c**. In particular, the spin states of the Fe1 site are roughly symmetrical (*o*-Fe_2P: 0.82 (up)/0.53(dn); *h*-Fe_2P: 0.34/0.96 states/eV-atom) while those of Fe2 site is asymmetric for both phases (*o*-Fe_2P: 0.49/1.10; *h*-Fe_2P: 0.19/1.49 states/eV-atom), as expected from asymmetry of the Fe2 site (square pyramidal). As a result, the calculated moments are lower for *o*-Fe_2P (Fe1: 0.24 μ_B, Fe2: 1.60 μ_B) than for *h*-Fe_2P (Fe1: 0.84 μ_B, Fe2: 2.18 μ_B) (**Table 2**). The non-magnetic DOS calculation results (**Figure S5)** showed that *o*-Fe_2P phase has a higher DOS at E_F (5.98 states/f.u.) than *h*-Fe_2P (4.82 states/f.u.).

4

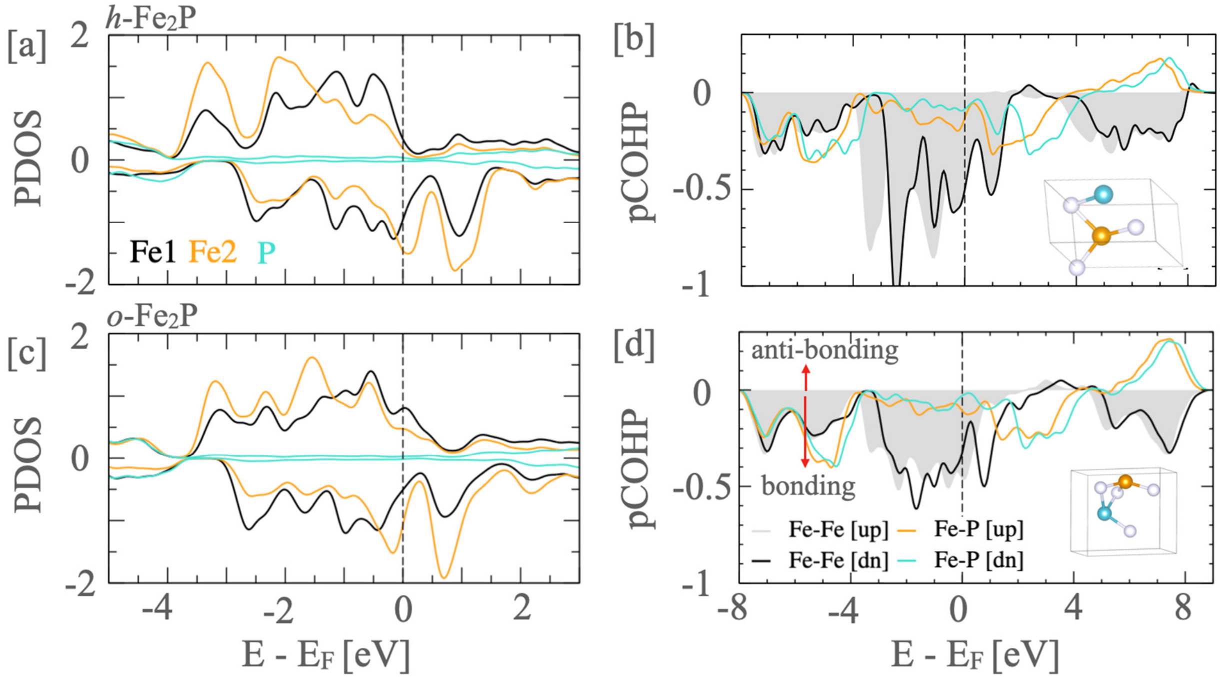

Figure 4. The partial density of states (PDOS) and projected crystal orbital Hamilton population (pCOHP) of Fe_2P in (a, b) hexagonal, and (c,d) orthorhombic structures. A negative (positive) sign in pCOHP indicates bonding (anti-bonding). The insets in (b,d) show a local motif used for the COHP calculations.

Table 2. Calculated and experimental magnetic moments for both polymorphs of Fe_2P.

	Calculated moment, μ_B				**Experimental moment, μ_B**	
Polymorph	**Fe1**	**Fe2**	**Total**	**Ratio h/o**	**Total**	**Ratio h/o**
***h*-Fe_2P**	0.84	2.18	3.02	1.64	2.48	1.70
***o*-Fe_2P**	0.24	1.60	1.84		1.46	

The projected crystal orbital Hamilton population (pCOHP) for Fe-Fe and Fe-P interactions in both the hexagonal and orthorhombic Fe_2P phases is shown in **Figures 4b,d**. In both phases, the Fe-P spin-down channel in *o*-Fe_2P shows a lower number of bonding states at E_F compared to up-spin. The overall distribution of bonding states in *o*-Fe_2P is more symmetric, i.e., weaker magnetic exchange that leads to reduced spin polarization. The weak exchange is also responsible for the depletion in bonding states at the E_F in *o*-Fe_2P (**Figure 4d**) compared to *h*-Fe_2P (**Figure 4c**). We hypothesize that the reduced number of bonding states at the E_F opens the space for enhancing HER activity. The major difference is in the degree of slope of pCOHP Fe-Fe [up] and Fe-P [up] spin channel in *o*-Fe_2P compared to *h*-Fe_2P. The higher degree of slope in *o*-Fe_2P suggests more thermally active electronic states near the Fermi-level. The presence of such states in *o*-Fe_2P give edge for metal-hydrogen functionalization, i.e., better H adsorption with higher probability for Fe-3d/P-3p orbital overlap with H-1s orbitals.

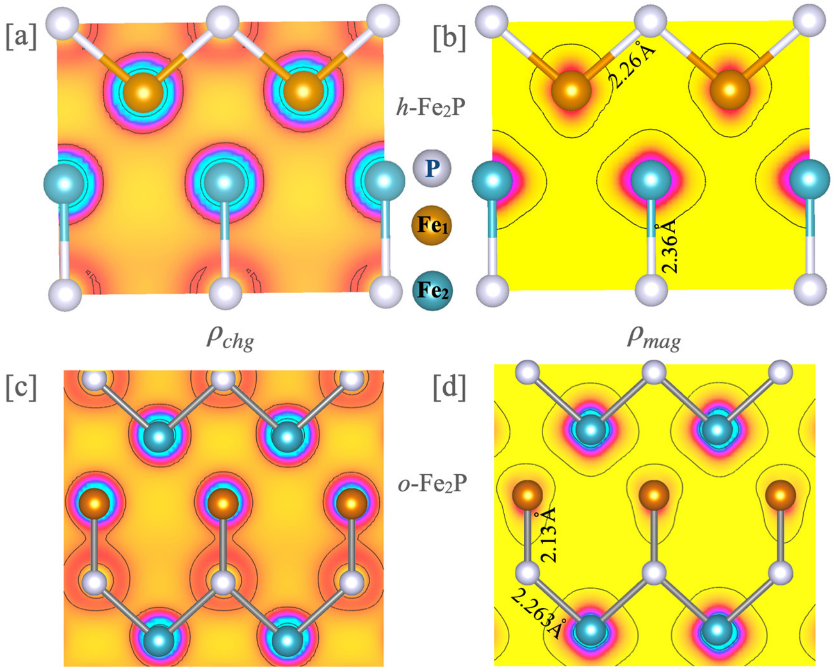

Figure 5. 2D projected charge and magnetization density in (a,b) orthorhombic and (c,d) hexagonal phases of Fe_2P. The isosurface value of 10^{-5} $e^-/Å^3$ was used. The shown interatomic distances are taken from the optimized crystal structures of both polymorphs.

The charge and magnetic density behavior in both Fe_2P polymorphs is shown in **Figure 5**. Upon analyzing local charge behavior, we found that in *o*-Fe_2P phase (**Figure 5c,d**), Fe1 pulls more charge (0.40e^-) from Fe2 while charges of Fe1 in *h*-Fe_2P phase (**Figure 5a,b**) remain almost spherical (0.39e^-). The observed charge disproportion at Fe1 vs. Fe2 is reflected through stronger Fe-P charge overlap in *o*-Fe_2P phase, which is also in line with trends in the shortest Fe1-P distances: Fe1-P distances are 2.19/2.24 Å in the orthorhombic structure while, in *h*-Fe_2P, the Fe1-P1/P2 distance are longer at 2.21/2.29 Å. The Fe charge reduction in *o*-Fe_2P is expected to reduce the strength of magnetic exchange interactions when compared with the hexagonal phase, which is reflected through smaller Fe moments in *o*-Fe_2P as shown in **Table 2**.

Transport and magnetic properties

The *h*-Fe_2P and *o*-Fe_2P powders were sintered into dense 4 mm pellets. No transformation of *o*-Fe_2P↔*h*-Fe_2P after SPS sintering was observed by PXRD analysis (**Figure S6**). From 2 K to 300 K, the electrical resistivity of two polymorphs were measured using a 4-probe configuration while thermal conductivity was measured in a 2-probe configuration. The resistivities of both polymorphs increase with temperature indicating metallic behavior (**Figures 6, S7)**, yet the shape of the curves is different from the usual *T*-linear dependence, expected for metals with dominant phonon scattering at temperatures above 20% of Debye temperature.[66] At 300 K, the electrical resistivities of *h*-Fe_2P and *o*-Fe_2P were estimated to be 9.2 μΩ•m and 16.7 μΩ•m, respectively. The reported value of resistivity for a *h*-Fe_2P single crystal is 4.3 μΩ•m along the *b* axis and 3.0 μΩ•m along the *c* axis.[17,67] The higher resistivity of our *h*-Fe_2P than the reported value could be due to grain boundaries of the pellet. The grain boundaries in sintered pellets may contribute to the difference in absolute values of resistivity for two polymorphs. Although the absolute value of resistivity of *o*-Fe_2P is higher than that of *h*-Fe_2P, the normalized resistivities lay on top of each other (**Figure 6a)**, indicating that the lattice distortion of *o*-Fe_2P has little impact on the resistivity behavior. Because of the metallic nature of both polymorphs, the Seebeck coefficients were low, less than 10 μV/K (data not shown due to instrumental limitations causing noisy nature of the measurement). At 300 K, the total thermal conductivities of *h*-Fe_2P and *o*-Fe_2P pellets were comparable, as shown in **Figure 6b**.

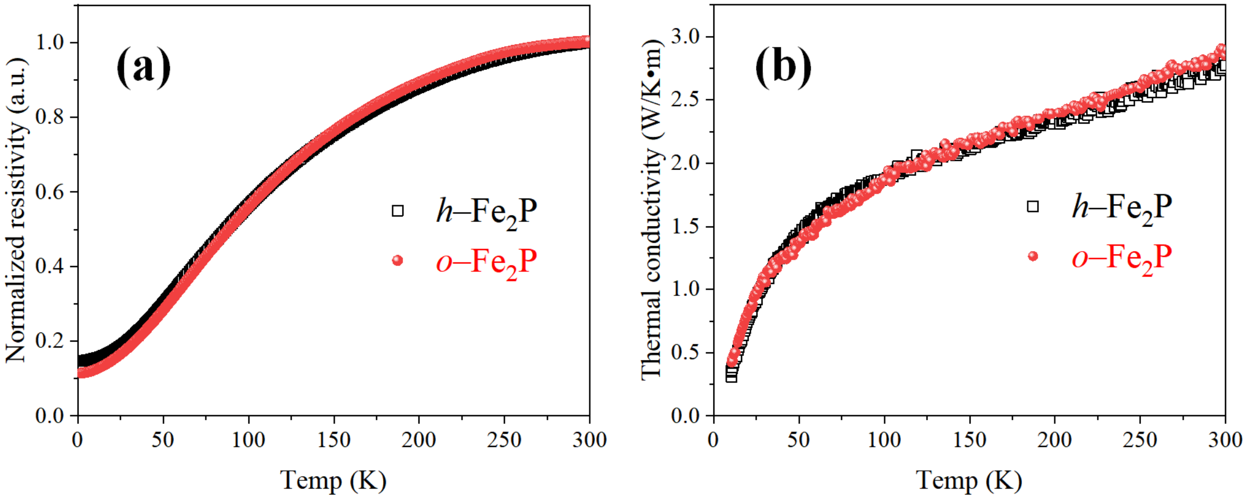

Figure 6. (a) Electrical resistivity normalized to the value at room temperature and (b) thermal conductivity of *h*-Fe_2P (black square) and *o*-Fe_2P (red circle) pellets.

In **Figure 7a**, the temperature dependences of magnetic susceptibility ($\chi = M/H$) are shown for the *h*-Fe_2P and *o*-Fe_2P samples under an applied field of 1000 Oe. Upon lowering temperature, the *h*-Fe_2P phase exhibits a sharp transition from paramagnetic to ferromagnetic state, consistent with previous reports.[68,69] The Curie temperature (T_C), derived from the local minimum value of the derivative of the χ vs T plot, was 212 K for the *h*-Fe_2P phase. The extrapolated value from $1/\chi$ dependence shows similar results (**Figure S8a**). The reported T_C of *h*-Fe_2P varies somewhat,[17,18,68,70,71] but the value determined for an Fe_2P polycrystalline sample was 216 K.[68] The *o*-Fe_2P polymorph orders ferromagnetically at a higher temperature of 248 K (**Figures 7a,S8a**). Distortion of the triangular Fe sublattice and shortening of Fe–Fe distances in the orthorhombic polymorph, as well as the strengthening of Fe-Fe interactions as indicated by charge density analysis, may be responsible for the increase in the ordering temperature by 36 K.

To connect DFT E_{form} to the observed $\Delta T_C = 36\ K$, an estimate of transition temperatures can be made from the energy differences between different structural and/or magnetic states.[72] While the

Curie temperature is better modeled by a paramagnetic (PM) state with finite moments but randomly oriented, it is beyond the current scope. Yet, given that there is a FM↔PM phase transition before the o-Fe_2P↔h-Fe_2P one, we can roughly estimate the difference ΔT_C by the energy difference between NM hexagonal and orthorhombic phases, i.e., $\Delta T_C \sim [\mathrm{E(NM\text{-}hex)} - \mathrm{E(NM\text{-}ortho)}]/k_B$, i.e., [(–327.5) – (–330.3)] meV/atom $/k_B$ ~ 32.5 K, similar to that 36 K found in experiments.

Both polymorphs exhibit isothermal field dependence of magnetization, which is typical for soft ferromagnets with almost no hysteresis at 2 K (**Figure 7b**) and paramagnetic-like dependence at room temperature (**Figure S8b**). At 2 K, the saturation magnetization of 1.24 μ_B/Fe for h-Fe_2P was achieved. Slightly larger value of 1.46 μ_B/Fe was reported for single crystals of h-Fe_2P.[17,68] Despite the higher ordering temperature, the saturation moment of o-Fe_2P was 40% lower, or 0.73 μ_B/Fe. This is in good agreement with the DFT results (**Table 2**), which predict the average magnetic moment of o-Fe_2P (0.92 μ_B/Fe) to be 39% lower than that for h-Fe_2P phase (1.51 μ_B/Fe). The ratio of magnetic moments (M_{hex}/M_{ortho}) are similar (exp. = 1.70, cal. = 1.64) (**Table 2**).

Combining the magnetic measurement results and DFT calculations, the o-Fe_2P phase has a lower moment on Fe atoms but a higher magnetic transition temperature than h-Fe_2P, likely due to shorter Fe-P and Fe-Fe distances and the corresponding strengthening of bonding (lowering of formation energy). Further studies using neutron diffraction are required to clarify the magnetic structure of the orthorhombic polymorph.[73,74] Due to the higher ordering temperature, the orthorhombic polymorph could be used as a base material to develop magnetic[74,75] or magnetocaloric materials through appropriate doping.[69,76] The undoped pristine o-Fe_2P phase exhibited a moderate magnetocaloric response of $-\Delta S = 2.2$ J/kg·K in 0-5 T range of the applied magnetic field (**Figure S9**).

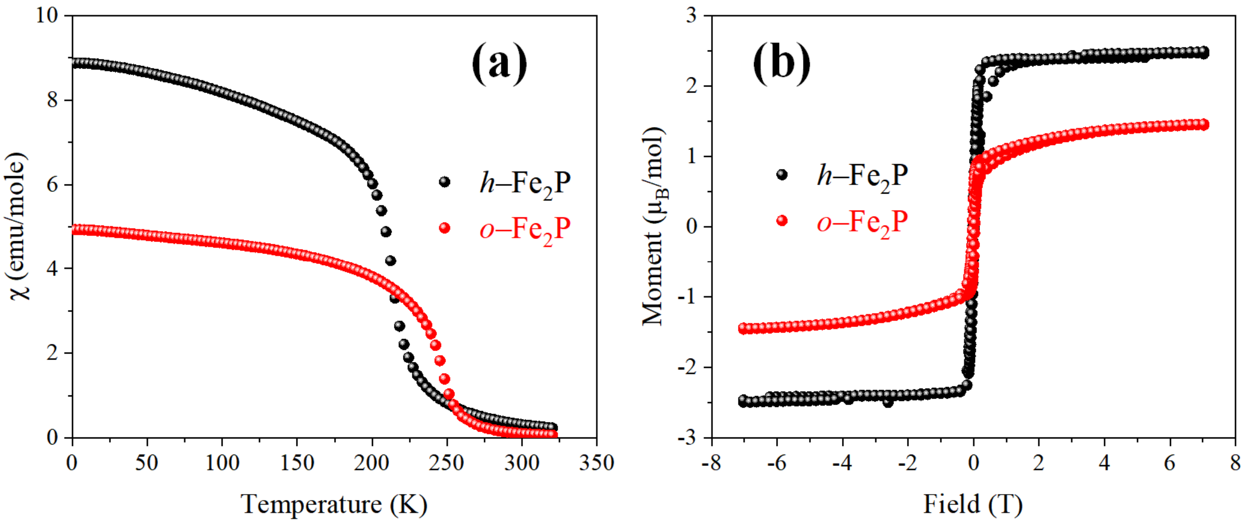

Figure 7. Magnetic properties of *h*-Fe_2P (black) and *o*-Fe_2P (red): (a) temperature dependence of magnetic susceptibility under an applied field of 1000 Oe, yielding $T_C = 212$ K for *h*-Fe_2P and $T_C = 248$ K for *o*-Fe_2P; and (b) isothermal magnetization at 2 K, yielding 1.24 μ_B/Fe for *h*-Fe_2P phase and 0.73 μ_B/Fe for *o*-Fe_2P phase.

Electrocatalytic properties

The comparative studies of polymorphs for electrocatalytic activity are quite rare.[46,77] Our previous report about two NiP_2 polymorphs shows that semiconducting/metallic nature of bulk structure affects the performance of catalysts in the hydrogen/oxygen evolution reactions (HER/OER).[46] As both Fe_2P polymorphs synthesized here are metallic with comparable resistivities, they could be good candidates to more precisely monitor the effect of bulk crystal and electronic structure on electrocatalytic activity. The working electrode was prepared by making an assembly with the 4 mm SPSed pellet attached to a gold wire, followed by molding it with insulating epoxy. The geometric densities of the two polymorph pellets were similar. **Figure 8a** shows the cathodic polarization curves recorded for the *h*-Fe_2P and *o*-Fe_2P catalysts in 0.5 M H_2SO_4 electrolyte at room temperature. To generate a current density $j = -10$ mA/cm^2, the overpotential $\eta_{10} = -214$ mV was estimated for *h*-Fe_2P. *o*-Fe_2P phase needed a 37% (or 80 mV) lower overpotential $\eta_{10} = -134$ mV than *h*-Fe_2P. Moreover, *o*-Fe_2P still shows the higher activity when it comes to η_{100} to drive current density $j = -100$ mA/cm^2, as it only needed $\eta_{100} = -269$ mV while *h*-Fe_2P requires $\eta_{100} = -393$ mV for this purpose. The Tafel slope represents the trend of the overpotential required to generate the current density by a factor of 10. The Tafel slope of *h*-Fe_2P was estimated to be

$b = 107$ mV/dec, while o-Fe_2P exhibits $b = 97$ mV/dec (**Figure 8b**), indicating the lower HER kinetic barrier of o-Fe_2P over h-Fe_2P. The relatively high overpotential and Tafel slopes of both polymorphs compared to other nanostructured Fe_2P HER catalysts are due to a smaller surface area of the dense pellet, which could represents a small deviation from the actual geometric area.[78] Nevertheless, the η_{10} value of h-Fe_2P is comparable to other reported reference Fe_2P catalysts (**Table S5**). The electrochemical impedance spectroscopy (EIS) was measured at -0.6 V_{SCE} (η_{40} of h-Fe_2P) for both catalysts. The Nyquist plot shows that the charge transfer resistance of h-Fe_2P (25 Ω) was higher than that for o-Fe_2P (7 Ω), in good agreement with superior HER performance of o-Fe_2P (**Figure S10**).

Given that the surfaces of the both catalysts are flat, as revealed by SEM studies **(Figure S11)**, and that the two Fe_2P polymorphs are expected to have the same number of adsorption sites and similar surface composition, the faster HER kinetics of o-Fe_2P may originate from the electronic structure of the materials. Both magnetic and non-magnetic DOS calculations showed that d-band center position for o-Fe_2P shifted a bit upward to the E_F (**Table S4**). This upshift of d-band center may promote orbital overlap between the metal and hydrogen by emptying the antibonding orbitals and results in balancing the adsorption energy.[79–82] Also, o-Fe_2P has a higher total and Fe-3d DOS at E_F than h-Fe_2P (**Figure S5**). There are not many reports on the effect of DOS at E_F for catalyst activity, but we hypothesize that the increment of electron carriers may contribute to facile HER kinetics. In our previous study of ternary $NiSi_{1-x}P_x$ catalysts, Ni_2SiP, which had a higher DOS at E_F than other P-rich Ni-Si-P compounds, was found to be the most efficient HER catalyst.[83] Lastly, as shown in the COHP results **(Figure 4)**, the positive slope of bonding state pCOHP curves at E_F for o-Fe_2P may indicate the possibility of enhanced Fe orbital overlap with hydrogen. The atomic configuration on the surface would also be an important factor for improved catalytic activity but is beyond the scope of the current study.

To test the electrocatalytic stability, accelerated degradation testing (ADT) was performed by conducting 1,000 cycles consecutively with a rate of 50 mV/s (**Figure 8c)**. Cycle-dependent cathodic polarization curves showed that both polymorphs showed a slightly lower overpotential at η_{10}, possibly due to surface reconstructions after the ADT. However, h-Fe_2P had a higher overpotential (cathodic shift) after –0.3 V, while o-Fe_2P showed almost identical overpotential at the higher potential region and demonstrated good stability during the 1,000 consecutive cycles.

To further evaluate the catalytic stability trend, chronopotentiometry (CP) was performed for 50 h, which measures the overpotential to generate a fixed current density of -10 mA/cm^2 for an extended period (**Figure 8d**). η_{10} values increased for both polymorphs after the 20 h of CP testing, by 10.7.% for *h*-Fe_2P and 9.7% for *o*-Fe_2P. This observation corroborates the reasonably good long-term stability of the Fe_2P catalysts and suggests comparable durability of both *o*-Fe_2P and *h*-Fe_2P during CP testing in acidic HER. The PXRD patterns of both polymorphs before and after HER stability testing showed that no phase transformation or decomposition occurred (**Figure S12**). From both stability tests, the η_{10} value of *o*-Fe_2P remained more than 80 mV lower than that of *h*-Fe_2P, confirming the superior HER activity of the orthorhombic phase. It's difficult to standardize the η_{10} value of a certain catalyst because it may vary depending on the different substrates, synthetic routes, and actual surface area, but *h*-Fe_2P, which is the reference catalyst in this study, displays an η_{10} value in a reasonable range to previous reports as shown in **Figure 9** and **Table 5**.[84–91] It is noteworthy that the structural distortion from the higher symmetry hexagonal to lower symmetry orthorhombic structure significantly enhances the HER activity of *o*-Fe_2P without an adjustment of composition via surface engineering or doping.

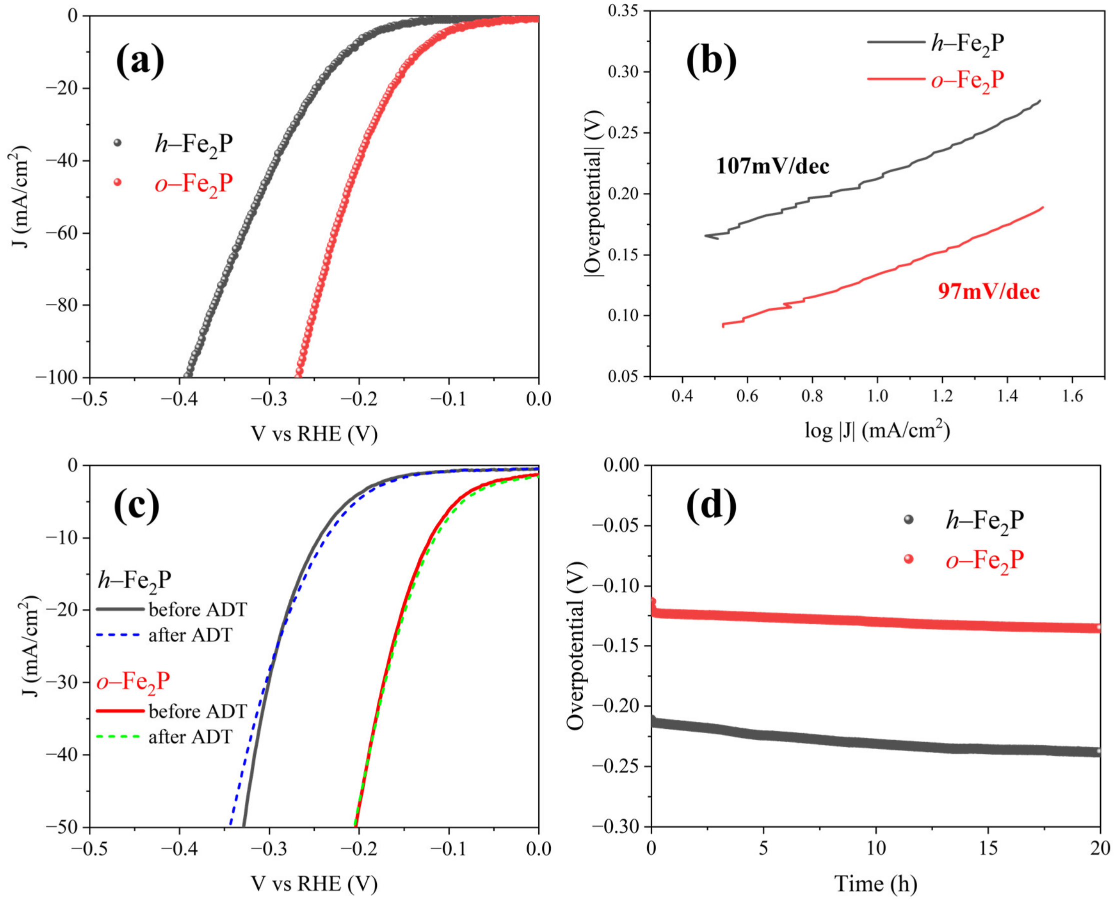

Figure 8. Cathodic polarization curves (a), as well as Tafel (b), ADT (c), and CP (d) plots for *h*-Fe_2P (black) and *o*-Fe_2P (red) polymorphs, all recorded in aq. 0.5 M H_2SO_4 at room temperature.

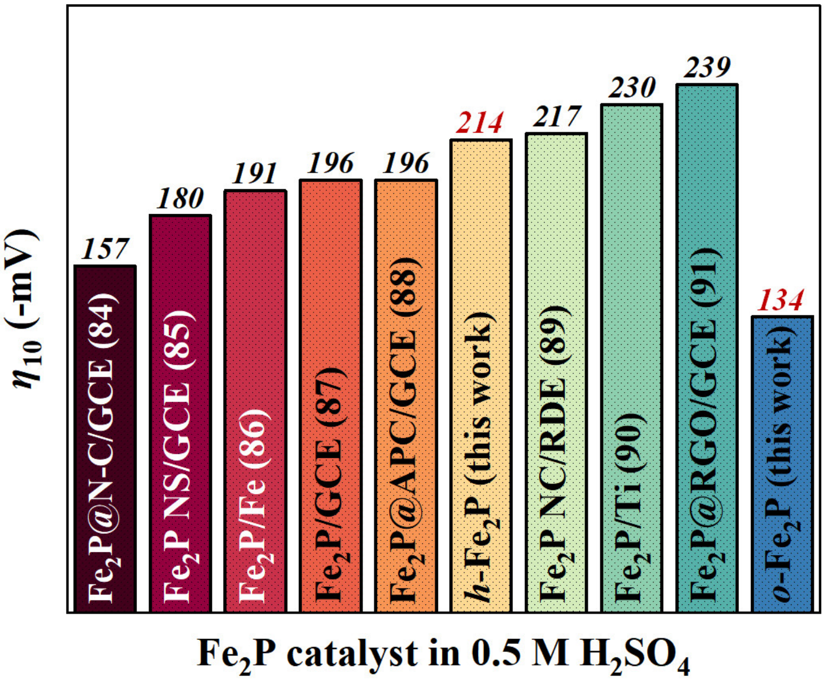

Figure 9. The reported η_{10} values of hexagonal Fe_2P HER catalysts in 0.5 M H_2SO_4 compared to the values for *h*-Fe_2P and *o*-Fe_2P produced in this study. The numbers in parentheses correspond to references.

Conclusion

Single-phase samples of the orthorhombic Fe_2P polymorph were prepared under ambient pressure using Sn-flux. *In situ* powder XRD analysis combined with DSC measurements demonstrate that the phase transition from *o*-Fe_2P to *h*-Fe_2P begins around 550°C while the reverse process is kinetically hindered. The two Fe_2P polymorphs have similar temperature dependencies of electrical resistivity and total thermal conductivity. However, their magnetic and catalytic properties are different. *o*-Fe_2P exhibits a 40% smaller saturation magnetic moment with a higher Curie temperature than *h*-Fe_2P. The spin-polarized density of states highlights that the origin of the lower magnetic moment of *o*-Fe_2P is from a more symmetrical distribution of spin-up and spin-down states at E_F. In terms of electrocatalytic properties, *o*-Fe_2P exhibits superior catalytic activity in acidic HER requiring a lower overpotential over the hexagonal polymorph with comparable long-term stability. Electronic-structure analyses suggests that the higher HER activity of *o*-Fe_2P is due to an upshift of the *d*-band center position, higher DOS at E_F, and more prominent antibonding nature of the shortest Fe-P interactions. In this study, we established reliable means to synthesize a low-temperature (more stable) Fe_2P polymorph and demonstrated how the associated structural distortion changes the electronic structure and consequently affects the physical, magnetic, and electrochemical properties between two Fe_2P polymorphs.

AUTHOR INFORMATION

Corresponding Author

Dr Kirill Kovnir, kovnir@iastate.edu

Author Contributions

The manuscript was written through contributions of all authors. All authors have given approval to the final version of the manuscript.

Funding Sources

This research was supported by the National Science Foundation Grant No. 1955456. The work at Ames National Laboratory (Y.M., P.S.) was supported by the DOE Office of Science, Basic Energy Sciences, Materials Science & Engineering Division. The Ames National Laboratory is operated for the U.S. DOE by Iowa State University under contract #DE-AC02-07CH11358. Use of the Advanced Photon Source was supported by U.S. Department of Energy, Office of Basic Energy Sciences, under Contract No. DE-AC02-06CH11357.

ACKNOWLEDGMENT

We are thankful to Dr. Wenqian Xu and Dr. Andrey Yakovenko (Argonne National Laboratory) for their help with collecting in-situ synchrotron XRD data and Dr. Julia Zaikina (ISU) for access to the Spark Plasma Sintering instrument.

REFERENCES

(1) Von Schnering, H. G.; Hoenle, W. Chemistry and Structural Chemistry of Phosphides and Polyphosphides. 48. Bridging Chasms with Polyphosphides. *Chem. Rev.* **1988**, *88* (1), 243–273.

(2) Chen, J.-H.; Whitmire, K. H. A Structural Survey of the Binary Transition Metal Phosphides and Arsenides of the D-Block Elements. *Coord. Chem. Rev.* **2018**, *355*, 271–327.

(3) Carenco, S.; Portehault, D.; Boissière, C.; Mézailles, N.; Sanchez, C. Nanoscaled Metal Borides and Phosphides: Recent Developments and Perspectives. *Chem. Rev.* **2013**, *113* (10), 7981–8065.

(4) Schöneich, M.; Hohmann, A.; Schmidt, P.; Pielnhofer, F.; Bachhuber, F.; Weihrich, R.; Osters, O.; Köpf, M.; Nilges, T. Element Allotropes and Polyanion Compounds of Pnicogenes and Chalcogenes: Stability, Mechanisms of Formation, Controlled Synthesis and Characterization. *Z. Für Krist. - Cryst. Mater.* **2017**, *232* (1–3), 91–105.

(5) Liu, X.; Yu, Z.; Liang, Q.; Zhou, C.; Wang, H.; Zhao, J.; Wang, X.; Yu, N.; Zou, Z.; Guo, Y. High-Pressure Crystal Growth, Superconducting Properties, and Electronic Band Structure of Nb_2P_5. *Chem. Mater.* **2020**, *32* (20), 8781–8788.

(6) Lee, S. J.; Viswanathan, G.; Carnahan, S. L.; Harmer, C. P.; Akopov, G.; Rossini, A. J.; Miller, G. J.; Kovnir, K. Add a Pinch of Tetrel: The Transformation of a Centrosymmetric Metal into a Nonsymmorphic and Chiral Semiconductor. *Chem. – Eur. J.* **2022**, *28* (9), e202104319.

(7) Quinn, R. J.; Bos, J.-W. G. Recent Progress in Phosphide Materials for Thermoelectric Conversion. *J. Mater. Chem. A* **2023**, *11* (16), 8453–8469.

(8) Yue, L.; Liang, J.; Wu, Z.; Zhong, B.; Luo, Y.; Liu, Q.; Li, T.; Kong, Q.; Liu, Y.; Asiri, A. M.; Guo, X.; Sun, X. Progress and Perspective of Metal Phosphide/Carbon Heterostructure Anodes for Rechargeable Ion Batteries. *J. Mater. Chem. A* **2021**, *9* (20), 11879–11907.

(9) Brock, S. L.; Perera, S. C.; Stamm, K. L. Chemical Routes for Production of Transition-Metal Phosphides on the Nanoscale: Implications for Advanced Magnetic and Catalytic Materials. *Chem. - Eur. J.* **2004**, *10* (14), 3364–3371.

(10) Brock, S. L.; Senevirathne, K. Recent Developments in Synthetic Approaches to Transition Metal Phosphide Nanoparticles for Magnetic and Catalytic Applications. *J. Solid State Chem.* **2008**, *181* (7), 1552–1559.

(11) Naher, M. I.; Naqib, S. H. A Comprehensive Study of the Thermophysical and Optoelectronic Properties of Nb_2P_5 via Ab-Initio Technique. *Results Phys.* **2021**, *28*, 104623.

(12) Liu, Y.; Wang, Y.; Song, S.; Zhang, H. Tumor Diagnosis and Therapy Mediated by Metal Phosphorus-Based Nanomaterials. *Adv. Mater.* **2021**, *33* (49), 2103936.

(13) Pu, Z.; Liu, T.; Amiinu, I. S.; Cheng, R.; Wang, P.; Zhang, C.; Ji, P.; Hu, W.; Liu, J.; Mu, S. Transition-Metal Phosphides: Activity Origin, Energy-Related Electrocatalysis Applications, and Synthetic Strategies. *Adv. Funct. Mater.* **2020**, *30* (45), 2004009.

(14) Zhang, H.; Maijenburg, A. W.; Li, X.; Schweizer, S. L.; Wehrspohn, R. B. Bifunctional Heterostructured Transition Metal Phosphides for Efficient Electrochemical Water Splitting. *Adv. Funct. Mater.* **2020**, *30* (34), 2003261.

(15) Li, Y.; Dong, Z.; Jiao, L. Multifunctional Transition Metal-Based Phosphides in Energy-Related Electrocatalysis. *Adv. Energy Mater.* **2020**, *10* (11), 1902104.

(16) Chiba, S. Magnetic Properties of Iron Phosphide Fe_2P. *J. Phys. Soc. Jpn.* **1960**, *15* (4), 581–585.

(17) Fujii, H.; Hōkabe, T.; Kamigaichi, T.; Okamoto, T. Magnetic Properties of Fe_2P Single Crystal. *J. Phys. Soc. Jpn.* **1977**, *43* (1), 41–46.

(18) Wautelet, M.; Gérard, A.; Grandjean, F.; De Strooper, K.; Robbrecht, G. Magnetic Properties of Fe_2P. *Phys. Status Solidi A* **1977**, *39* (2), 425–430.

(19) Scheerlinck, D.; Legrand, E. Neutron Diffraction Study of the Magnetic Structure of Fe_2P. *Solid State Commun.* **1978**, *25* (3), 181–184.

(20) Tobola, J.; Bacmann, M.; Fruchart, D.; Kaprzyk, S.; Koumina, A.; Niziol, S.; Soubeyroux, J.-L.; Wolfers, P.; Zach, R. Magnetism of Fe_2P Investigated by Neutron Experiments and Band Structure Calculations. *J. Magn. Magn. Mater.* **1996**, *157–158*, 708–710.

(21) Caron, L.; Hudl, M.; Höglin, V.; Dung, N. H.; Gomez, C. P.; Sahlberg, M.; Brück, E.; Andersson, Y.; Nordblad, P. Magnetocrystalline Anisotropy and the Magnetocaloric Effect in Fe_2P. *Phys. Rev. B* **2013**, *88* (9), 094440.

(22) Fruchart, R.; Roger, A.; Senateur, J. P. Crystallographic and Magnetic Properties of Solid Solutions of the Phosphides M_2P, M = Cr, Mn, Fe, Co, and Ni. *J. Appl. Phys.* **1969**, *40* (3), 1250–1257.

(23) Carlsson, B.; Gölin, M.; Rundqvist, S. Determination of the Homogeneity Range and Refinement of the Crystal Structure of Fe_2P. *J. Solid State Chem.* **1973**, *8* (1), 57–67.

(24) Tegus, O.; Brück, E.; Buschow, K. H. J.; De Boer, F. R. Transition-Metal-Based Magnetic Refrigerants for Room-Temperature Applications. *Nature* **2002**, *415* (6868), 150–152.

(25) Buseck, P. R. Phosphide from Meteorites: Barringerite, a New Iron-Nickel Mineral. *Science* **1969**, *165* (3889), 169–171.

(26) Skála, R.; Císařová, I. Crystal Structure of Meteoritic Schreibersites: Determination of Absolute Structure. *Phys. Chem. Miner.* **2005**, *31* (10), 721–732.

(27) Pratesi, G. Icosahedral Coordination of Phosphorus in the Crystal Structure of Melliniite, a New Phosphide Mineral from the Northwest Africa 1054 Acapulcoite. *Am. Mineral.* **2006**, *91* (2–3), 451–454.

(28) Britvin, S. N.; Rudashevsky, N. S.; Krivovichev, S. V.; Burns, P. C.; Polekhovsky, Y. S. Allabogdanite, $(Fe,Ni)_2P$, a New Mineral from the Onello Meteorite: The Occurrence and Crystal Structure. *Am. Mineral.* **2002**, *87* (8–9), 1245–1249.

(29) Britvin, S. N.; Shilovskikh, V. V.; Pagano, R.; Vlasenko, N. S.; Zaitsev, A. N.; Krzhizhanovskaya, M. G.; Lozhkin, M. S.; Zolotarev, A. A.; Gurzhiy, V. V. Allabogdanite, the High-Pressure Polymorph of $(Fe,Ni)_2P$, a Stishovite-Grade Indicator of Impact Processes in the Fe–Ni–P System. *Sci. Rep.* **2019**, *9* (1), 1047.

(30) Dera, P.; Lavina, B.; Borkowski, L. A.; Prakapenka, V. B.; Sutton, S. R.; Rivers, M. L.; Downs, R. T.; Boctor, N. Z.; Prewitt, C. T. High-Pressure Polymorphism of Fe_2P and Its Implications for Meteorites and Earth's Core. *Geophys. Res. Lett.* **2008**, *35* (10), L10301.

(31) Gu, T.; Wu, X.; Qin, S.; McCammon, C.; Dubrovinsky, L. Probing Nonequivalent Sites in Iron Phosphide Fe2P and Its Mechanism of Phase Transition. *Eur. Phys. J. B* **2013**, *86* (7), 311.

(32) Zhao, Z.; Liu, L.; Zhang, S.; Yu, T.; Li, F.; Yang, G. Phase Diagram, Stability and Electronic Properties of an Fe–P System under High Pressure: A First Principles Study. *RSC Adv.* **2017**, *7* (26), 15986–15991.

(33) Litasov, K. D.; Bekker, T. B.; Sagatov, N. E.; Gavryushkin, P. N.; Krinitsyn, P. G.; Kuper, K. E. $(Fe,Ni)_2P$ Allabogdanite Can Be an Ambient Pressure Phase in Iron Meteorites. *Sci. Rep.* **2020**, *10* (1), 8956.

(34) Senateur, J. P.; Rouault, A.; Fruchart, R.; Capponi, J. J.; Perroux, M. Etude Par Spectrometrie Mossbauer Des Transformations Cristallographiques Sous Hautes Pressions de MnFeAs et Fe_2P. *Mater. Res. Bull.* **1976**, *11* (6), 631–635.

(35) Severin, L.; Haggstrom, L.; Nordstrom, L.; Andersson, Y.; Johansson, B. Magnetism and Crystal Structure in Orthorhombic Fe_2P: A Theoretical and Experimental Study. *J. Phys. Condens. Matter* **1995**, *7* (1), 185–198.

(36) Wu, X.; Qin, S. First-Principles Calculations of the Structural Stability of Fe_2P. *J. Phys. Conf. Ser.* **2010**, *215*, 012110.

(37) Bhat, S. S.; Gupta, K.; Bhattacharjee, S.; Lee, S.-C. Role of Zero-Point Effects in Stabilizing the Ground State Structure of Bulk Fe_2P. *J. Phys. Condens. Matter* **2018**, *30* (21), 215401.

(38) Henge, D. B.; Hermus, M.; Litterscheid, C. F.; Wagner, N.; Beck, J.; Albert, B.; Brgoch, J. Discovery of γ-MnP_4 and the Polymorphism of Manganese Tetraphosphide. *Inorg. Chem.* **2015**, *54* (17), 8761–8768.

(39) Stoyko, S. S.; Blanchard, P. E. R.; Ramachandran, K. K.; Mar, A. Quaternary Rare-Earth Transition-Metal Phosphides $REMnCuP_2$ (RE = Y, La–Nd, Sm, Gd–Tm, Lu) with $CaAl_2Si_2$-Type Structure and a Polymorph of $LaMnCuP_2$ with $BaCu_2S_2$-Type Structure. *J. Solid State Chem.* **2019**, *269*, 100–106.

(40) Akopov, G.; Mark, J.; Viswanathan, G.; Lee, S. J.; McBride, B. C.; Won, J.; Perras, F. A.; Paterson, A. L.; Yuan, B.; Sen, S.; Adeyemi, A. N.; Zhang, F.; Wang, C.-Z.; Ho, K.-M.; Miller, G. J.; Kovnir, K. Third Time's the Charm: Intricate Non-Centrosymmetric Polymorphism in LnSiP$_3$ (Ln = La and Ce) Induced by Distortions of Phosphorus Square Layers. *Dalton Trans.* **2021**, *50* (19), 6463–6476.

(41) Eisenburger, L.; Weippert, V.; Paulmann, C.; Johrendt, D.; Oeckler, O.; Schnick, W. Discovery of Two Polymorphs of TiP_4N_8 Synthesized from Binary Nitrides. *Angew. Chem.* **2022**, *134* (19).

(42) Solozhenko, V. L.; Matar, S. F. Polymorphism of Boron Phosphide: Theoretical Investigation and Experimental Assessment. *J. Mater. Chem. C* **2022**, *10* (10), 3937–3943.

(43) Sun, Y.; Lin, C.; Chen, J.; Xu, F.; Yang, S.; Li, B.; Yang, G.; Luo, M.; Ye, N. α-Ca_2CdP_2 and β-Ca_2CdP_2: Two Polymorphic Phosphide-Based Infrared Nonlinear Crystals with Distorted NLO-Active Tetrahedral Motifs Realizing Large Second Harmonic Generation Effects and Suitable Band Gaps. *Inorg. Chem.* **2021**, *60* (10), 7553–7560.

(44) Bither, T. A.; Prewitt, C. T.; Gillson, J. L.; Bierstedt, P. E.; Flippen, R. B.; Young, H. S. New Transition Metal Dichalcogenides Formed at High Pressure. *Solid State Commun.* **1966**, *4* (10), 533–535.

(45) Hull, G. W.; Hulliger, F. $CuSe_2$, a Marcasite Type Superconductor. *Nature* **1968**, *220* (5164), 257–258.

(46) Owens-Baird, B.; Xu, J.; Petrovykh, D. Y.; Bondarchuk, O.; Ziouani, Y.; González-Ballesteros, N.; Yox, P.; Sapountzi, F. M.; Niemantsverdriet, H.; Kolen'ko, Y. V.; Kovnir, K. NiP_2: A Story of Two Divergent Polymorphic Multifunctional Materials. *Chem. Mater.* **2019**, *31* (9), 3407–3418.

(47) Wang, J.; Dolyniuk, J.-A.; Kovnir, K. Unconventional Clathrates with Transition Metal–Phosphorus Frameworks. *Acc. Chem. Res.* **2018**, *51* (1), 31–39.

(48) Cicirello, G.; Wang, M.; Sam, Q. P.; Hart, J. L.; Williams, N. L.; Yin, H.; Cha, J. J.; Wang, J. Two-Dimensional Violet Phosphorus P_{11}: A Large Band Gap Phosphorus Allotrope. *J. Am. Chem. Soc.* **2023**, *145* (14), 8218–8230.

(49) Kanatzidis, M. G.; Pöttgen, R.; Jeitschko, W. The Metal Flux: A Preparative Tool for the Exploration of Intermetallic Compounds. *Angew. Chem. Int. Ed.* **2005**, *44* (43), 6996–7023.

(50) Nakajima, Y.; Araki, S.; Kinoshita, D.; Hirose, K.; Tateno, S.; Kawaguchi, S. I.; Hirao, N. New Pressure-Induced Phase Transition to Co_2Si-Type Fe_2P. *Am. Mineral.* **2020**, *105* (11), 1752–1755.

(51) Dera, P.; Lazarz, J. D.; Lavina, B. Pressure-Induced Development of Bonding in NiAs Type Compounds and Polymorphism of NiP. *J. Solid State Chem.* **2011**, *184* (8), 1997–2003.

(52) Dera, P.; Nisar, J.; Ahuja, R.; Tkachev, S.; Prakapenka, V. B. New Type of Possible High-Pressure Polymorphism in NiAs Minerals in Planetary Cores. *Phys. Chem. Miner.* **2013**, *40* (2), 183–193.

(53) Sheldrick, G. M. Crystal Structure Refinement with *SHELXL*. *Acta Crystallogr. Sect. C Struct. Chem.* **2015**, *71* (1), 3–8.

(54) Toby, B. H.; Von Dreele, R. B. *GSAS-II* : The Genesis of a Modern Open-Source All Purpose Crystallography Software Package. *J. Appl. Crystallogr.* **2013**, *46* (2), 544–549.

(55) Kresse, G.; Hafner, J. Norm-Conserving and Ultrasoft Pseudopotentials for First-Row and Transition Elements. *J. Phys. Condens. Matter* **1994**, *6* (40), 8245–8257.

(56) Hafner, J. *Ab-Initio* Simulations of Materials Using VASP: Density-Functional Theory and Beyond. *J. Comput. Chem.* **2008**, *29* (13), 2044–2078.

(57) Perdew, J. P.; Burke, K.; Ernzerhof, M. Generalized Gradient Approximation Made Simple. *Phys. Rev. Lett.* **1996**, *77* (18), 3865–3868.

(58) Maintz, S.; Deringer, V. L.; Tchougréeff, A. L.; Dronskowski, R. Analytic Projection from Plane-Wave and PAW Wavefunctions and Application to Chemical-Bonding Analysis in Solids. *J. Comput. Chem.* **2013**, *34* (29), 2557–2567.

(59) Maintz, S.; Deringer, V. L.; Tchougréeff, A. L.; Dronskowski, R. LOBSTER: A Tool to Extract Chemical Bonding from Plane-Wave Based DFT: Tool to Extract Chemical Bonding. *J. Comput. Chem.* **2016**, *37* (11), 1030–1035.

(60) Dronskowski, R.; Bloechl, P. E. Crystal Orbital Hamilton Populations (COHP): Energy-Resolved Visualization of Chemical Bonding in Solids Based on Density-Functional Calculations. *J. Phys. Chem.* **1993**, *97* (33), 8617–8624.

(61) Hoffmann, R. *Solids and Surfaces: A Chemist's View of Bonding in Extended Structures*; VCH publishers Inc., New York, 1998.

(62) Dronskowski, R. *Computational Chemistry of Solid State Materials*; Wiley-VCH, Weinheim, New York, 2005.

(63) Coleman, N.; Lovander, M. D.; Leddy, J.; Gillan, E. G. Phosphorus-Rich Metal Phosphides: Direct and Tin Flux-Assisted Synthesis and Evaluation as Hydrogen Evolution Electrocatalysts. *Inorg. Chem.* **2019**, *58* (8), 5013–5024.

(64) Liyanage, I. A.; Flores, A. V.; Gillan, E. G. Tunable Synthesis of Metal-Rich and Phosphorus-Rich Nickel Phosphides and Their Comparative Evaluation as Hydrogen Evolution Electrocatalysts. *Inorg. Chem.* **2023**, *62* (12), 4947–4959.

(65) Ellner, M.; Mittemeijer, E. J. The Reconstructive Phase Transformation β-Co_2P → α-Co_2P and the Structure of the High-Temperature Phosphide β-Co_2P. *Z. Für Anorg. Allg. Chem.* **2001**, *627* (9), 2257.

(66) Wang, J.; Dolyniuk, J.-A.; Krenkel, E. H.; Niedziela, J. L.; Tanatar, M. A.; Timmons, E. I.; Lanigan-Atkins, T.; Zhou, H.; Cheng, Y.; Ramirez-Cuesta, A. J.; Schlagel, D. L.; Kaluarachchi, U. S.; Wang, L.-L.; Bud'ko, S. L.; Canfield, P. C.; Prozorov, R.; Delaire, O.; Kovnir, K. Clathrate $BaNi_2P_4$: An Interplay of Heat and Charge Transport Due to Strong Host–Guest Interactions. *Chem. Mater.* **2020**, *32* (18), 7932–7940.

(67) Yin, Y.; Zhai, K.; Zhang, B.; Zhai, S. Electrical Resistivity of Iron Phosphides at High-Pressure and High-Temperature Conditions With Implications for Lunar Core's Thermal Conductivity. *J. Geophys. Res. Solid Earth* **2019**, *124* (6), 5544–5556.

(68) Leif Lundgren; Gulzar Tarmohamed; Olof Beckman; Bertil Carlsson; Stig Rundqvist. First Order Magnetic Phase Transition in Fe_2P. *Phys. Scr.* **1978**, *17* (1), 39–48.

(69) He, A.; Svitlyk, V.; Mozharivskyj, Y. Synthetic Approach for $(Mn,Fe)_2(Si,P)$ Magnetocaloric Materials: Purity, Structural, Magnetic, and Magnetocaloric Properties. *Inorg. Chem.* **2017**, *56* (5), 2827–2833.

(70) Wäppling, R.; Häggström, L.; Ericsson, T.; Devanarayanan, S.; Karlsson, E.; Carlsson, B.; Rundqvist, S. First Order Magnetic Transition, Magnetic Structure, and Vacancy Distribution in Fe_2P. *J. Solid State Chem.* **1975**, *13* (3), 258–271.

(71) Nagase, S.; Watanabe, H.; Shinohara, T. Magnetic Properties of the System Fe_2P-Mn_2P. *J. Phys. Soc. Jpn.* **1973**, *34* (4), 908–910.

(72) Zarkevich, N. A.; Johnson, D. D. Reliable Thermodynamic Estimators for Screening Caloric Materials. *J. Alloys Compd.* **2019**, *802*, 712–722.

(73) Zhuravlev, I. A.; Antropov, V. P.; Vishina, A.; Van Schilfgaarde, M.; Belashchenko, K. D. Tunable Dimensional Crossover and Magnetocrystalline Anisotropy in Fe_2P -Based Alloys. *Phys. Rev. Mater.* **2017**, *1* (5), 051401.

(74) He, Y.; Adler, P.; Schneider, S.; Soldatov, I.; Mu, Q.; Borrmann, H.; Schnelle, W.; Schaefer, R.; Rellinghaus, B.; Fecher, G. H.; Felser, C. Intrinsic Magnetic Properties of a Highly Anisotropic Rare-Earth-Free Fe_2P-Based Magnet. *Adv. Funct. Mater.* **2022**, *32* (4), 2107513.

(75) Guillou, F.; Sun-Liting; Haschuluu, O.; Ou, Z. Q.; Brück, E.; Tegus, O.; Yibole, H. Room Temperature Magnetic Anisotropy in Fe_2P-Type Transition Metal Based Alloys. *J. Alloys Compd.* **2019**, *800*, 403–411.

(76) Rudolph, K.; Pathak, A. K.; Mudryk, Y.; Pecharsky, V. K. Magnetostructural Phase Transitions and Magnetocaloric Effect in $(Gd_{5-x}Sc_x)Si_{1.8}Ge_{2.2}$. *Acta Mater.* **2018**, *145*, 369–376.

(77) McGlynn, J. C.; Cascallana-Matías, I.; Fraser, J. P.; Roger, I.; McAllister, J.; Miras, H. N.; Symes, M. D.; Ganin, A. Y. Molybdenum Ditelluride Rendered into an Efficient and Stable Electrocatalyst for the Hydrogen Evolution Reaction by Polymorphic Control. *Energy Technol.* **2018**, *6* (2), 345–350.

(78) Wu, T.; Stone, M. L.; Shearer, M. J.; Stolt, M. J.; Guzei, I. A.; Hamers, R. J.; Lu, R.; Deng, K.; Jin, S.; Schmidt, J. R. Crystallographic Facet Dependence of the Hydrogen Evolution Reaction on CoPS: Theory and Experiments. *ACS Catal.* **2018**, *8* (2), 1143–1152.

(79) Hammer, B.; Norskov, J. K. Why Gold Is the Noblest of All the Metals. *Nature* **1995**, *376* (6537), 238–240.

(80) Nilsson, A.; Pettersson, L. G. M.; Hammer, B.; Bligaard, T.; Christensen, C. H.; Norskov, J. K. The Electronic Structure Effect in Heterogeneous Catalysis. *Catal. Lett.* **2005**, *100* (3–4), 111–114.

(81) Sun, S.; Zhou, X.; Cong, B.; Hong, W.; Chen, G. Tailoring the D-Band Centers Endows $(Ni_xFe_{1-x})_2P$ Nanosheets with Efficient Oxygen Evolution Catalysis. *ACS Catal.* **2020**, *10* (16), 9086–9097.

(82) Wang, B.; Zhang, F. Main Descriptors To Correlate Structures with the Performances of Electrocatalysts. *Angew. Chem. Int. Ed.* **2022**, *61* (4), e202111026.

(83) Kong, S.; Singh, P.; Akopov, G.; Jing, D.; Davis, R.; Perez-Aguilar, J.; Hong, J.; Lee, S. J.; Viswanathan, G.; Soto, E.; Azhan, M.; Fernandes, T.; Harycki, S.; Gundlach-Graham, A.; Kolen'ko, Y. V.; Johnson, D. D.; Kovnir, K. Probing of the Noninnocent Role of P in Transition-Metal Phosphide Hydrogen Evolution Reaction Electrocatalysts via Replacement with Electropositive Si. *Chem. Mater.* **2023**, *35* (14), 5300–5310.

(84) Gong, Y.; Xu, L.-H.; Zhang, X.-J.; Cosnier, S.; Shan, D. Phytic Acid-Assisted Hollow Fe_2P/N-C Nanoshuttle Derived from NH_2MIL: Synthesis Strategy and Electrochemical Application for Hydrogen Evolution. *J. Alloys Compd.* **2023**, *947*, 169418.

(85) Zhang, Y.; Zhang, H.; Feng, Y.; Liu, L.; Wang, Y. Unique Fe_2P Nanoparticles Enveloped in Sandwichlike Graphited Carbon Sheets as Excellent Hydrogen Evolution Reaction Catalyst and Lithium-Ion Battery Anode. *ACS Appl. Mater. Interfaces* **2015**, *7* (48), 26684–26690.

(86) Read, C. G.; Callejas, J. F.; Holder, C. F.; Schaak, R. E. General Strategy for the Synthesis of Transition Metal Phosphide Films for Electrocatalytic Hydrogen and Oxygen Evolution. *ACS Appl. Mater. Interfaces* **2016**, *8* (20), 12798–12803.

(87) Yang, J.; Ouyang, Y.; Zhang, H.; Xu, H.; Zhang, Y.; Wang, Y. Novel Fe_2P/Graphitized Carbon Yolk/Shell Octahedra for High-Efficiency Hydrogen Production and Lithium Storage. *J. Mater. Chem. A* **2016**, *4* (25), 9923–9930.

(88) Yao, Y.; Mahmood, N.; Pan, L.; Shen, G.; Zhang, R.; Gao, R.; Aleem, F.; Yuan, X.; Zhang, X.; Zou, J.-J. Iron Phosphide Encapsulated in P-Doped Graphitic Carbon as Efficient and Stable Electrocatalyst for Hydrogen and Oxygen Evolution Reactions. *Nanoscale* **2018**, *10* (45), 21327–21334.

(89) Shin, D.; Kim, H. J.; Kim, M.; Shin, D.; Kim, H.; Song, H.; Choi, S.-I. $Fe_xNi_{2-x}P$ Alloy Nanocatalysts with Electron-Deficient Phosphorus Enhancing the Hydrogen Evolution Reaction in Acidic Media. *ACS Catal.* **2020**, *10* (19), 11665–11673.

(90) Liu, M.; Yang, L.; Liu, T.; Tang, Y.; Luo, S.; Liu, C.; Zeng, Y. Fe_2P/Reduced Graphene Oxide/Fe_2P Sandwich-Structured Nanowall Arrays: A High-Performance Non-Noble-Metal Electrocatalyst for Hydrogen Evolution. *J. Mater. Chem. A* **2017**, *5* (18), 8608–8615.

(91) Wang, K.; Tan, J.; Lu, Z.; Chen, S.; She, X.; Zhang, H.; Yang, D. Nanoscale Engineering MoP/Fe_2P/RGO toward Efficient Electrocatalyst for Hydrogen Evolution Reaction. *Int. J. Hydrog. Energy* **2018**, *43* (30), 13939–13945.